scientific reports

Check for updates

OPEN

Phosphorus-doped T-graphene nanocapsule toward O_3 and SO_2 gas sensing: a DFT and QTAIM analysis

Mohammad Tanvir Ahmed[1]✉, Abdullah Al Roman[1], Debashis Roy[1], Shariful Islam[2] & Farid Ahmed[2]

Tetragonal graphene nano-capsule (TGC), a novel stable carbon allotrope of sp^2 hybridization is designed and doped with phosphorus (P) to study the O_3 and SO_2 gas sensitivity via density functional theory calculation. Real frequencies verified the natural existence of both TGC and P-doped TGC (PTGC). Both TGC and PTGC suffer structural deformations due to interaction with O_3 and SO_2 gases. The amount of charge transfer from the adsorbent to the gas molecule is significantly greater for O_3 adsorption than SO_2 adsorption. The adsorption energies for TGC + O_3 and PTGC + O_3 complexes are − 3.46 and − 4.34 eV respectively, whereas for TGC + SO_2 and PTGC + SO_2 complexes the value decreased to − 0.29 and − 0.30 eV respectively. The dissociation of O_3 is observed via interaction with PTGC. A significant variation in electronic energy gap and conductivity results from gas adsorption which can provide efficient electrical responses via gas adsorption. The blue/red shift in the optical response proved to be a way of detecting the types of adsorbed gases. The adsorption of O_3 is exothermic and spontaneous whereas the adsorption of SO_2 is endothermic and non-spontaneous. The negative change in entropy verifies the thermodynamic stability of all the complexes. QTAIM analysis reveals strong covalent or partial covalent interactions between absorbent and adsorbate. The significant variation in electrical and optical response with optimal adsorbent-gas interaction strength makes both TGC and PTGC promising candidates for O_3 and SO_2 sensing.

Keywords T-graphene, DFT, Adsorption, Toxic gas, Quantum dot

Environmental contamination caused by industrial wastes and other byproducts has increased as a result of rapid industrialization. Many dangerous gases, including those produced by motorized traffic, power plants, industry, biological waste, and other sources, are present in the environment[1]. These gases include CH_4, CO, SO_2, CO_2, NO, NH_3, CH_3OH, H_2S, O_3, PH_3, and $COCl_2$[2–4]. The well-known air contaminant ozone (O_3) has negative effects on the mucosa in the eyes and respiratory tissues. The lung is the primary target of tropospheric ozone in humans, which has detrimental effects on bodily functions[5]. Another common type of air pollution is sulfur dioxide (SO_2), which is colorless, corrosive, and highly excitant. The interaction of SO_2 with the surrounding air can cause several concerns to human health as well as harmful effects on the environment[4]. Monitoring these dangerous gases is crucial for creating a healthier living environment, which is what spurred the advancement of innovative techniques for sensing these gases. A sensing material demonstrates an alteration in resistivity/conductivity due to charge transfer between the adsorbent and gas molecules[6,7].

The numerous bonding modes of carbon (C) atoms, which are widely dispersed in nature, allow them to form a broad variety of allotropes with distinct physical and chemical characteristics, including diamond carbon nanotubes, fullerene, graphene, and so on[8]. However, for toxic gas detection, pure graphene is too chemically inert and insensitive to be of much value[2], which led the researchers to study the sensitivity of various allotropes of C in both pristine and doped states for gas sensing applications[8–15]. P-doped graphene showed strong chemisorption of SO_2, NO_2, O_2, etc.[14]. According to the theoretical investigation of Yu et al., O_3 gas decomposes to O_2 gas via interaction with P- and N-doped graphene[10]. Pt-doped graphene showed strong adsorption of O_3 compared to SO_2[15].

Fullerene showed a high sensitivity toward H_2S, CH_4, C_3H_8, etc. toxic gases in theoretical and experimental investigations[13]. The presence of several gases, e.g., NO_2, NH_3, and so on can alter the conductivity of carbon nanotube (CNT) significantly[16]. The sensitivity of CNT for NH_3, NO_2, etc. toxic gases has enhanced when decorated with metal[11,12]. Compared to all other anticipated graphene variants, including the newly produced

[1]Department of Physics, Jashore University of Science and Technology, Jashore 7408, Bangladesh. [2]Department of Physics, Jahangirnagar University, Dhaka 1342, Bangladesh. ✉email: tanvir.phy43@gmail.com

graphene and graphdiyne, tetragonal graphene (T-graphene) is thermodynamically substantially more stable[17]. Very few studies on T-graphene's applications have been reported yet. T-graphene has shown high potential for gas sensing and ion storage applications[8,18,19]. Xie et al. reported T-graphene to be a potential candidate for NO and NO_2 detection[8]. Li-doped T-graphene is reported to be a promising material for H_2 adsorption and storage[19]. Liu et al. also reported that Li doping can improve the CO detection sensitivity of T-graphene[20].

Here, we have designed and optimized a new geometries, T-graphene capsule (TGC) quantum dot (QD) and P-doped TGC (PTGC) QD using density functional theory (DFT) calculations. The adsorption of O_3 and SO_2 toxic gases on both TGC and PTGC has been studied for gas sensing applications. The variation in structural, electronic, optical, and thermodynamic properties due to the interaction of TGC and PTGC with selected gas molecules has been investigated. The nature of the adsorbent-adsorbate interaction has been understood via the quantum theory of atoms in molecules (QTAIM) analysis. Since TGC is a novel geometry of carbon, the gas-sensing application of TGC and PTGC has not been studied yet.

Computational details

The nanocapsules of TGC and PTGC QDs are designed via "GaussView 06" and optimized to stable ground state energies by DFT calculation in "Gaussian 09W" software. For geometry optimization, we used the dispersion-corrected B3LYP-D3 functional with the 6-31G(d) basis set which can provide a good estimation of adsorption energies in the study[3]. The energy and frequency calculations were performed to understand the optical response and dynamic stability of the geometries. For a better estimation of the energy gap, the HSEH1PBE hybrid functional with LanL2DZ basis set was employed[21]. The stable configurations of the adsorbent + gas complex were chosen using the Adsorption Locator module[22,23]. The adsorption energy (E_{ads}) of the adsorbent + gas complexes were calculated via Eq. (1),

$$E_{ads} = E_{complex} - E_{capsule} - E_{gas}, \tag{1}$$

where, $E_{complex}$, $E_{capsule}$, and E_{gas} represent the energy of the complex structures, capsules, and gas molecules respectively[24,25]. The basis set superposition error (BSSE) in the electronic structure of molecules occurs when orbitals are approximated using the expansion of basis functions, and this has to be examined. The corresponding energy of BSSE (E_{BSSE}) were calculated via counterpoise method[26,27]. The adsorption energies of the complexes can be corrected using the following equation[3,28].

$$E_{ads\_BSSE} = E_{ads} + E_{BSSE}, \tag{2}$$

where E_{ads_BSSE} represents the BSSE-corrected adsorption energy.

The cohesive energy (E_C) of the adsorbents was estimated by Eq. (3)[29],

$$E_C = \frac{E_{Adbnt} - \sum_x n_x E_x}{\sum_x n_x}, \tag{3}$$

where, E_{Adbnt}, E_x, and n_x represent the adsorbent energy, energy of individual (x) species, and number of x species. The Mulliken charges (MC), electrostatic potential map (EPM), partial density of states (PDOS), highest occupied molecular orbital (HOMO), lowest unoccupied molecular orbital (LUMO), and energy gap of the geometries were studied to understand the electronic characteristics of the structures. The vital electronic parameters and global indices are calculated by the following set of equations[30–32].

$$E_f = \frac{1}{2}(E_H + E_L), \tag{4}$$

$$E_g = E_L - E_H \tag{5}$$

$$\Upsilon = \frac{E_g}{2}, \tag{6}$$

$$\Omega = \frac{E_L + E_H}{2}, \tag{7}$$

$$\lambda = \frac{1}{2\Theta}, \tag{8}$$

$$\xi = \frac{v^2}{2\Theta}, \tag{9}$$

where E_L, E_H, E_f, E_g, Υ, Ω, λ, and ξ represent the HOMO's energy, LUMO's energy, fermi energy, energy gap (HOMO–LUMO gap), global hardness, chemical potential, global softness, and electrophilicity index, respectively.

The variation in thermodynamic parameters i.e., enthalpy (H), Gibbs free energy (G), and entropy (S) can be calculated from the following relations[21].

$$\Delta\Psi = \Psi_{complex} - \Psi_{capsule} - \Psi_{gas}, \tag{10}$$

$$\Delta S = \frac{1}{T}(\Delta H - \Delta G), \tag{11}$$

where, $\Psi_{complex}$, $\Psi_{capsule}$, and Ψ_{gas} represent H/G of the complex structures, the adsorbent, and the gas molecules. $\Delta\Psi$ denotes enthalpy variation (ΔH) or free energy variation (ΔG). The nature of the gas-adsorbent interactions was understood via QTAIM analysis using the AIMALL package[33].

Results and discussion

Geometry analysis

The designed T-graphyne capsule (TGC) and P-doped T-graphyne capsule (PTGC) contain a total of 56 atoms (Fig. 1) possessing cohesive energies of − 8.42 and − 8.35 eV respectively suggesting a strong binding of the molecules. The average C–C bond length of the TGC QD is analogous to that of graphene, T-graphene, and CNT[34,35]. P-doping results in a significant structural deformation due to the higher atomic radius of P. Table 1 shows the variation in bond lengths between elements due to the adsorption of O_3 gases. The values in the parenthesis represent the bond lengths before adsorption. The adsorption of O_3 results in a significant deformation of TGC proven by the excessive changes in bond lengths. On the other hand, comparatively smaller variation in C–C bond lengths is observed due to PTGC + O_3 interaction. However, the C–P bond lengths change to a great extent after adsorption. It is observed that the O_3 molecule dissociates into O_2 and oxygenates PTGC. The SO_2 gas molecule shows lesser interaction with TGC and PTGC compared to O_3. Very slight deformation is observed in the molecules via nominal variation in C–C, C–P, and S=O bond lengths. SO_2 does not reveal any dissociation of molecules like O_3. The SO_2 gas molecule shows lesser interaction with TGC and PTGC compared to O_3. Very slight deformation is observed in the molecules via nominal variation in C–C, C–P, and S=O bond lengths. SO_2 does not reveal any dissociation of molecules like O_3.

Adsorption analysis

The adsorption energy (E_{ads}) represents the amount of energy required to separate the adsorbate from the adsorbent surface. Both the adsorbents show exothermic adsorption of the selected gas molecules. O_3 shows very strong adsorption in both TGC and PTGC quantum dots. Although, SO_2 shows weaker interaction than O_3, the adsorption energies are still suitable for sensing application. The adsorption energies for O_3 are significantly higher on the selected adsorbents than on B-doped graphene[36], Pt-decorated graphene[15], $B_{12}N_{12}$ nanocage[37], and MoS_2[38]. Whereas TGC and PTGC show comparatively stronger adsorption of SO_2 than B-doped graphene[36], terthiophene[39], $B_{12}N_{12}$ nanocage[37], and $B_{12}P_{12}$ nanoclusters[40] adsorbents.

One of the vital characteristics of the adsorbent for sensing applications is the recovery time (τ). The recovery time can be calculated from Eq. (12)[2,3].

$$\tau = \frac{1}{f_r} e^{-\frac{E_{ads}}{K_b T}}, \tag{12}$$

where, f_r is the frequency of the irradiated electromagnetic (EM) wave. In experiments, the UV radiation (f_r =10^{12}–10^{14} Hz) is used for regenerating adsorbents. The temperature (T) of 298 K is used in this study.

The TGC + SO_2 and PTGC + SO_2 complexes show a recovery time of 2.7 ns and 3.23 ns suggesting a fast recovery via UV irradiation at room temperature makes both adsorbents suitable candidates for SO_2 adsorption. On the other hand, due to high adsorption energies, both TGC + O_3 and PTGC + O_3 complexes possess a high recovery time (Table 2). The recovery time remains impractical upon X-ray irradiation at 600 K temperature suggesting that the adsorbents cannot be recoverable via the conventional irradiation technique. In this circumstance, the adsorbents may regenerate through chemical reactions. Some of the commonly used regenerating agents e.g., HCl, NaOH, HNO_3, $NaHCO_3$, etc. may show better performance in recovering both adsorbents which require further investigations[21,41].

Vibrational properties

The frequency analysis reveals the vibrational modes in the molecular systems along with their dynamic stability. The TGC, PTGC and all their complexes possess real frequencies (Fig. 2) signifying all the geometries are stable and can exist in nature[42,43]. The IR peaks near 1528–1539 cm^{-1} indicate C–C stretching in the normal direction to the capsule length, whereas the peak near 1747 cm^{-1} represents C–C stretching along the capsule length. A P–C vibration of the PTGC molecule is observed near 1290 cm^{-1}. Through the adsorption of toxic gases, a slight variation in the peak position is observed due to the structural deformation. In the TGC + O_3 complex, O–O–O bending, O–O asymmetric stretching, O–O symmetric stretching and C–O stretching are observed at 633, 727, 916, and 1025 cm^{-1}, respectively. The peaks near 502 and 1129 cm^{-1} represent O=S=O bending and S=O stretching, respectively in the TGC + SO_2 complex. On the other hand, 499 and 1127 cm^{-1} peaks indicate the O=S=O bending and S=O stretching in the PTGC + SO_2 complex. Due to the dissociation of O_3 in the PTGC + O_3 complex, O=O stretching and P=O stretching is observed near 1653 and 1249 cm^{-1}, respectively.

Electronic properties

Electronic properties can provide significant information about the sensitivity of the adsorbents toward the selected gases[44,45]. Figure 3 shows the Mulliken charge distribution of the gas molecules, adsorbents and complexes. The central Oxygen (O) atom acts as the electron donor in the O_3 molecule, whereas in the SO_2 molecule

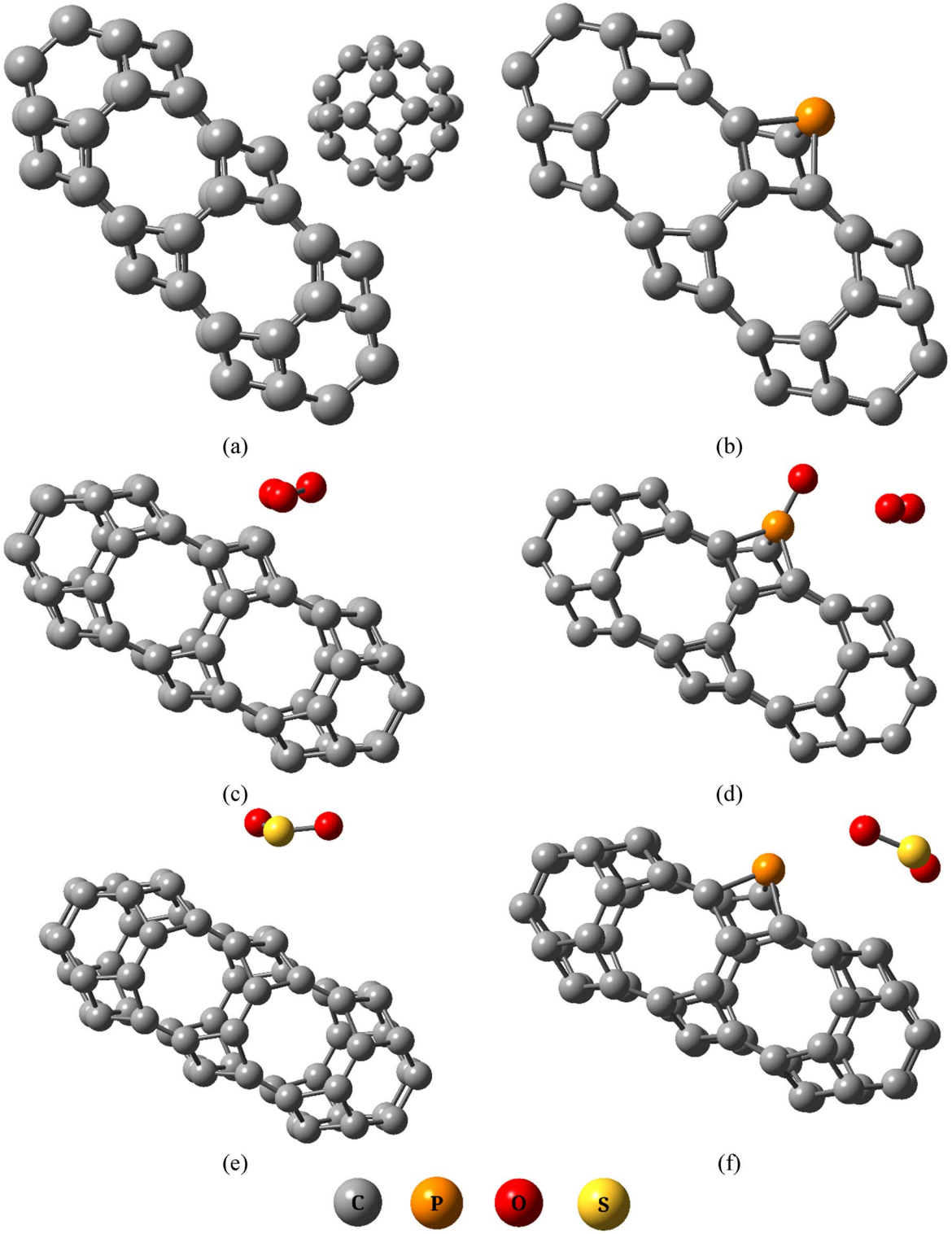

Figure 1. Optimized geometries of (**a**) TGC, (**b**) PTGC, (**c**) TGC + O_3, (**d**) PTGC + O_3, (**e**) TGC + SO_2, and (**f**) PTGC + SO_2.

electrons are shifted toward O atoms due to their high electronegativity. The Mulliken charges of all carbon (C) atoms are almost neutral in the TGC structure resulting in no net charge transfer between atoms. A significant charge transfer is observed in the TGC + O_3 complex with C atoms acting as electron donors. However, no notable change in color distribution in observed due to SO_2 adsorption on TGC, suggesting a nominal charge displacement.

The PTGC QD showed charge asymmetry since the electronegativity of C is greater than that of P. Hence, P–C bonding electrons are displaced toward C resulting in partially negative C atoms and partially positive P

Structures	C–C	C–P	O–O	S=O
TGC	1.416	–	–	–
TGC + O_3	1.474	–	1.448 (1.264)	–
TGC + SO_2	1.420	–	–	1.466 (1.464)
PTGC	1.422	1.862	–	–
PTGC + O_3	1.425	1.831	1.214	–
PTGC + SO_2	1.421	1.864	–	1.465

Table 1. Average bond lengths (Å) of the structures.

Complexes	E_{ads} (eV)	E_{ads_BSSE} (eV)	Recovery time (s)
TGC + O_3	− 3.46	− 3.19	7.41×10^{39}
TGC + SO_2	− 0.29	− 0.20	2.70×10^{-09}
PTGC + O_3	− 4.34	− 4.28	1.47×10^{58}
PTGC + SO_2	− 0.30	− 0.21	3.23×10^{-09}

Table 2. Adsorption energy and recovery time of the studied complexes.

atom. A strong negative charge transfer from adsorbent to O_3 molecule is demonstrated by a significant variation in the color of P and O atoms. Two oxygen atoms almost become charge neutral whereas electrons are shifted toward the 3rd O atom from P. This significant change displacement results in a strong adsorbent-adsorbate interaction. A very slight change in charge of the P atom is observed due to the interaction with SO_2 gas, suggesting a nominal charge transfer between absorbent and absorbate as observed in on TGC adsorbent, resulting in a weak attraction of SO_2.

Figure 4 shows the overall charge transfer toward gas molecules via adsorbate-adsorbent interaction. The maximum charge transfer on O_3 molecule occurs on TGC adsorbent whereas PTGC shows more charge transfer compared to TGC toward SO_2.

Figure 5 demonstrates the electrostatic potential map (EPM) of the absorbents and complexes. is an indispensable tool for deciphering the electrostatic potential arising from the arrangement of electrons and nuclei within a molecule, thereby allowing for the identification of potential reaction sites for both electrophilic and nucleophilic attacks. The red region indicates the negative potential i.e., the electron-rich region whereas the blue region represents the electron deficit region or positive potential region. The TGC adsorbent is almost neutral resulting in a uniform distribution of negative and positive charges. On the other hand, due to the asymmetry of charge distribution in the PTGC, the P-site region becomes a comparatively stronger electrophilic attack zone. The interaction with O_3 and SO_2, the O-site region demonstrates to be a more electron-rich region due to the high electronegativity of the O atom. The S-site region shows comparatively positive potential due to low electron density. The noticeable color change in both TGC and PTGC upon adsorption indicates a substantial charge transfer, implying a robust adsorbent-adsorbate interaction.

Figures 6 and 7 show the HOMOs and LUMOs TGC and PTGC along with their complexes respectively. Both HOMO and LUMO are localized in the TGC after gas adsorption. A nominal contribution to HOMO and LUMO is localized on the O_3 molecule adsorbed on TGC. On the other hand, a significant localization of LUMO was observed on the SO_2 molecule of the PTGC + SO_2 complex. Both adsorbents demonstrate a significant change in HOMOs and LUMOs due to toxic gas adsorption signifying strong interaction with notable charge transfer. The energies of HOMOs and LUMOs in the geometries are presented in Table 3.

The PDOS spectra are analyzed for a thorough understanding of electronic properties' variation (Fig. 8). The TGC showed an energy gap of 1.18 eV making it suitable for numerous semiconducting applications (Table 3). P-doping results in a low energy gap semiconductor through energy gap tuning. The energies of HOMOs and LUMOs of both adsorbents suffer a significant variation due to gas adsorption, resulting in an alteration of the energy gap. It is observed that the energies HOMOs of both TGC and PTGC significantly decrease after gas adsorption (Table 3), whereas the LUMO energies increase due to O_3 adsorption but decrease through SO_2 adsorption. The O and S atoms do not demonstrate any contribution to HOMOs and LUMOs of TGC and PTGC (except PTGC + SO_2, where a significant orbital contribution of both O and S are observed at LUMO). The observed PDOS spectra justify the HOMO and LUMO representation in Figs. 6 and 7. Figure 9 shows the variation in the energy gap of TGC and PTGC due to the interaction with gas molecules.

The variation in the energy gap can be a result of the variation in charge distribution and structural deformation in the adsorption process[21,46]. The change in energy gap results in a variation of electronic conductivity (EC) which follows the Eq. (13).

$$\sigma \propto e^{-\frac{E_g}{2K_bT}} \tag{13}$$

where, K_b and T represent the Boltzmann constant and absolute temperature[3]. The change in conductivity can provide a significant electrical response due to gas adsorption which makes TGC and PTGC potential materials

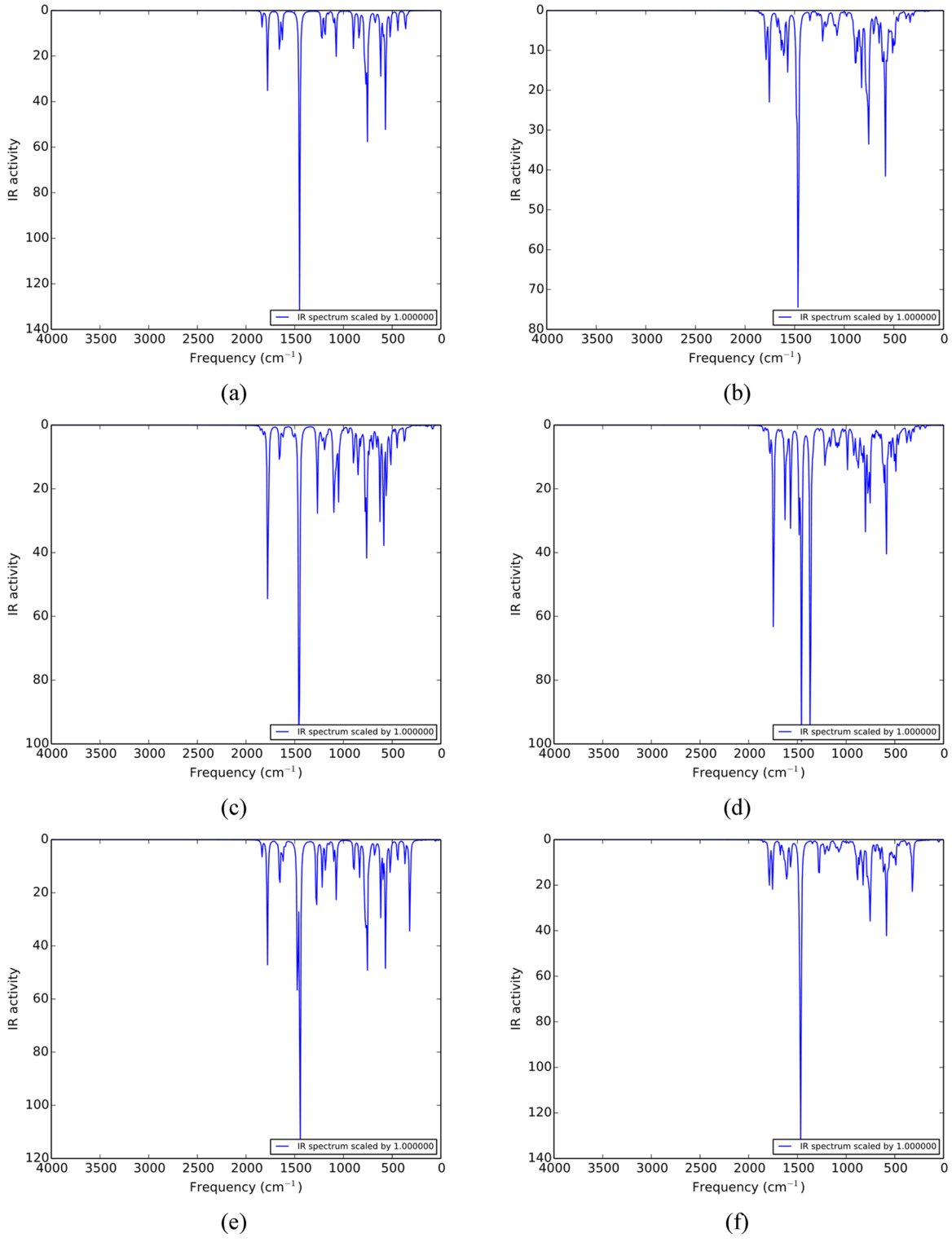

Figure 2. IR spectra of (**a**) TGC, (**b**) PTGC, (**c**) TGC + O_3, (**d**) PTGC + O_3, (**e**) TGC + SO_2, and (**f**) PTGC + SO_2 structures.

for O_3 and SO_2 sensing. Through proper calibration of EC, the adsorbent can be of use in the detection of the type of adsorbed gas.

The work function (φ), which is the energy needed to remove an electron from the fermi level and bring it to the vacuum, is a surface-dependent characteristic of the adsorbents. The materials' conductivity is impacted by changes in work function[47]. The work function is related to the fermi energy by the following equation,

$$\varphi = \left| V_{\infty+} - E_f \right| \tag{14}$$

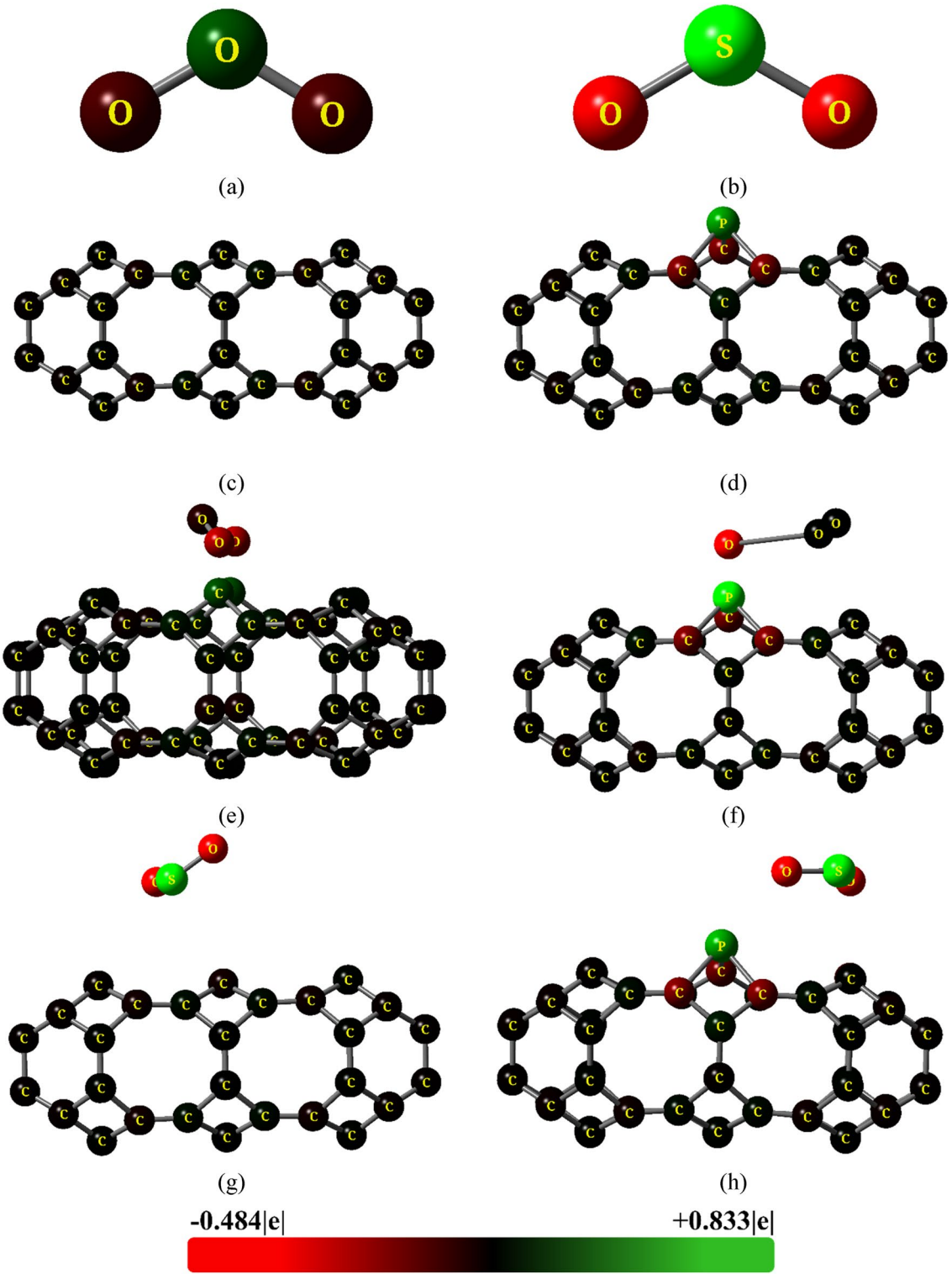

Figure 3. Mulliken charge distributions of (**a**) O_3, (**b**) SO_2, (**c**) TGC, (**d**) PTGC, (**e**) TGC + O_3, (**f**) PTGC + O_3, (**g**) TGC + SO_2, and (**h**) PTGC + SO_2.

where, $V_{\infty+}$ is the electrostatic potential of an electron far away from the adsorbent's surface. Table 3 shows that φ varies significantly via gas interaction suggesting a significant change in conductivity of the adsorbents. The change in current conduction via φ variation can be obtained via the Richardson–Dushman relation,

$$J = A_R T^2 e^{-\frac{\varphi}{K_b T}}, \tag{15}$$

where, J and A_R are the emitted electron density and the Richardson constant, respectively[48].

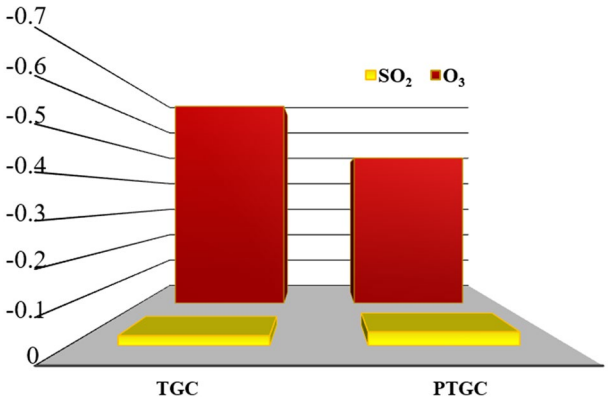

Figure 4. Mulliken charge transfer between adsorbent and gas molecules.

Global indices

Several reactivity parameters such as hardness, softness, chemical potential, and electrophilicity are calculated and their numerical values are given in Table 4. The corresponding values of Chemical hardness and electrophilicity, respectively, are small and large as compared to various carbon and boron nitride nanostructures while the chemical potential values are quite similar[49–51]. All the complexes of TGC and PTGC offer negative chemical potential value indicating their structural stability. The chemical hardness is a measure of opposition to charge transfer from a material whereas the softness signifies its opposite characteristic[52]. The hardness of TGC is increased slightly after absorption of O_3 and SO_2 indicating chemical stability upon gas adsorption. P doping reduces the value of hardness to about half that of its pristine structure. Although O_3 adsorption causes PTGC to almost regain the hardness of its pristine form, SO_2 adsorption dramatically declines the hardness and hence increases the chemical reactivity of PTGC which is also ensured by the very large value of electrophilicity.

Thermal properties

The thermodynamic stability of the complex structures can be understood from the change in enthalpy, Gibbs free energy, and entropy[26]. Their corresponding values after the adsorption of O_3 and SO_2 are tabulated in Table 5. The change in enthalpy (ΔH) upon O_3 adsorption for both TGC and PTGC are found to be − 3.15 and − 4.07 eV/atom respectively which signify that their interactions are exothermic and the bonding between the atoms of TGC + O_3 and PTGC + O_3 are more stable. Similarly, the change in Gibbs free energies (ΔG) is also negative for O_3 adsorption and positive for SO_2 adsorption which implies that O_3 adsorption is a spontaneous process whereas SO_2 adsorption is a non-spontaneous process[26,53]. The interaction of SO_2 with TGC and PTGC is endothermic with a ΔH value of 0.005 and 0.01 eV/atom respectively.

Entropy is a measure of a molecule's freedom of motion. It is higher when the product molecules have greater freedom of motion and is less positive if the product molecules are more ordered. The change in entropy due to the adsorption of O_3 and SO_2 on both TGC and PTGC is negative indicating that the complexes are thermodynamically ordered and stable[21,54].

Optical properties

The molar absorption coefficient (ε), as determined through UV–visible response analysis for all structures, is presented in Fig. 10. Both pristine configurations displayed a significant absorption coefficient (AC) with a strong absorption peak in the visible wavelength region. PTGC shows strong absorption in higher wavelength regions compared to TGC, verifying the smaller energy gap of PTGC than TGC. The strong absorption in the visible wavelength region makes both TGC and PTGC potential candidates for optoelectronic research. An increased optical responsiveness at a particular wavelength is correlated with a greater AC. In both adsorbents, gas adsorption is shown to cause a significant change in the AC spectra. Along with the variation in the intensity of AC, a significant red/blue shifting of the absorption peak is observed due to the interaction with gas molecules. The reflectivity of the is related to the AC by the following equations,

$$Abs = C\varepsilon l, \tag{16}$$

$$Abs = -\log(Tra), \tag{17}$$

$$Ref = 1 - \sqrt{(Tra)e^{Abs}}, \tag{18}$$

where *Abs*, *C*, *l*, *Tra*, and *Ref* indicate the absorbance, concentration, material thickness, transmittance, and reflectance, respectively[21].

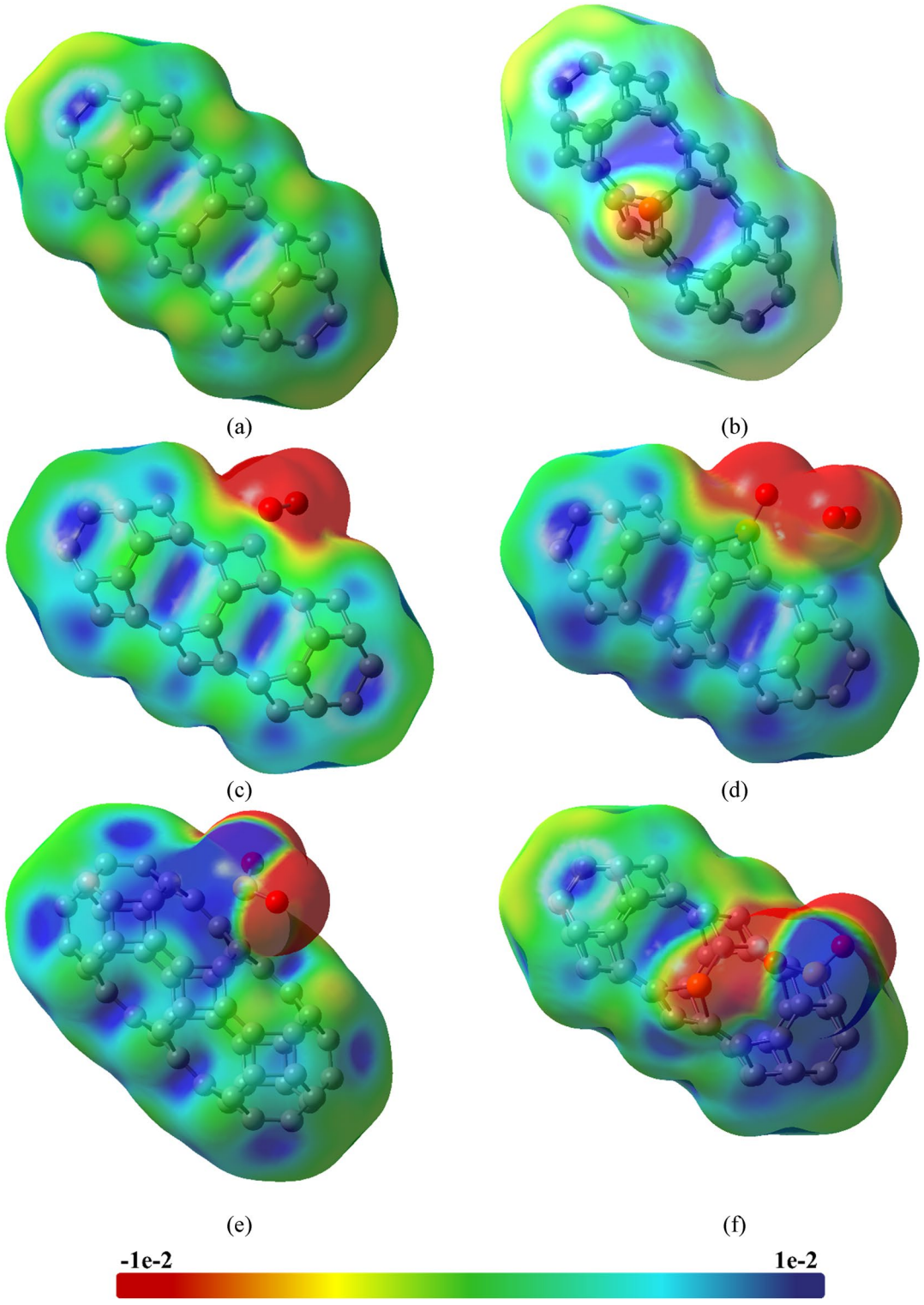

Figure 5. Electrostatic potential map of (**a**) TGC, (**b**) PTGC, (**c**) TGC + O_3, (**d**) PTGC + O_3, (**e**) TGC + SO_2, and (**f**) PTGC + SO_2.

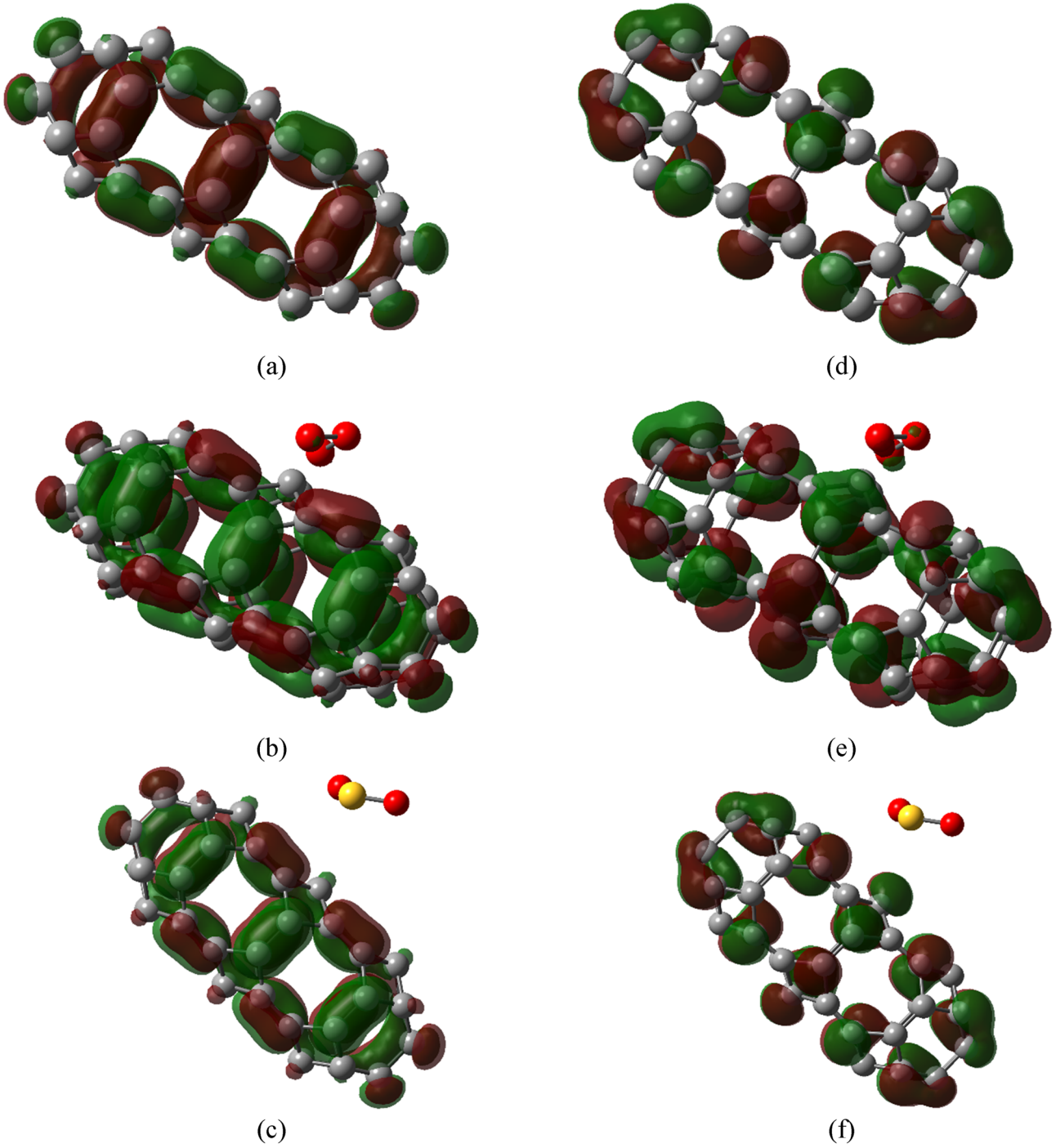

Figure 6. HOMOs of (**a**) TGC, (**b**) TGC + O_3, (**c**) TGC + SO_2, and LUMOs of (**d**) TGC, (**e**) TGC + O_3, (**f**) TGC + SO_2.

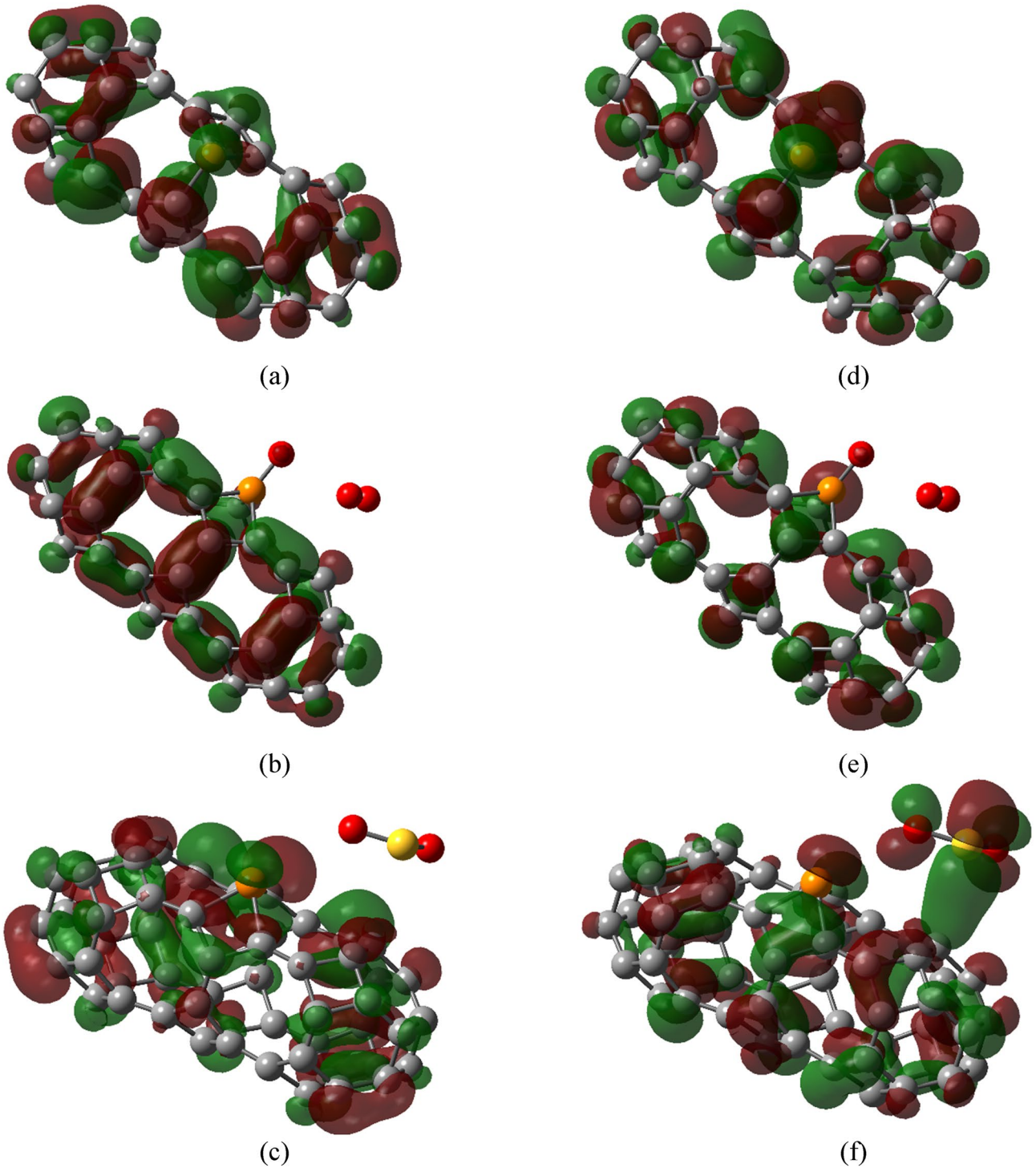

Figure 7. HOMOs of (**a**) PTGC, (**b**) PTGC + O_3, (**c**) PTGC + SO_2, and LUMOs of (**d**) PTGC, (**e**) PTGC + O_3, (**f**) PTGC + SO_2.

Structures	E_H (eV)	E_L (eV)	E_g (eV)	φ (eV)
TGC	− 6.16	− 4.98	1.18	5.57
TGC + O_3	− 6.24	− 4.96	1.28	5.6
TGC + SO_2	− 6.3	− 5.11	1.19	5.705
PTGC	− 4.8	− 4.18	0.62	4.49
PTGC + O_3	− 4.87	− 3.88	0.99	4.375
PTGC + SO_2	− 4.85	− 4.69	0.16	4.77

Table 3. E_H, E_L, E_g, and φ of the structures in the unit of eV.

As a result, a red/blue shift in AC likewise produces a red/blue shift in the structure's reflectivity, changing its color; in other words, adsorbents may change color by gas adsorption. Consequently, color fluctuation may be used to identify and detect the type of toxic gas adsorbed on TGC or PTGC.

QTAIM analysis

To gain a profound understanding of the nature and strength of molecular interactions, an in-depth Quantum Theory of Atoms in Molecules (QTAIM) analysis was performed on all complex structures. Figure 11 illustrates the molecular graph of these structures, with the green spots indicating the bond critical (BC) point. This BC point is crucial for assessing and ensuring the strength of intermolecular bonds. Hence, to characterize different types of interactions, descriptors including electron density (ρ_e),

$\nabla^2(\rho_e)$, electron's kinetic energy density (ED) (G_e), potential ED (V_e), and total ED (H_e) have been acquired at bond critical (BC) points (Table 6).

The presence of BC points in a molecule validates the creation of chemical bonds between the adsorbent and gas molecules and verifies that electron density is being transferred. The atoms in a molecule bind strongly and covalently if the values both $\nabla^2(\rho_e)$ and H_e found are negative, whereas for $\nabla^2(\rho_e) > 0$ and $H_e > 0$, the interaction is weak and electrostatic[31,32]. On the other hand, the bonding nature is partially covalent for $\nabla^2(\rho_e) > 0$ but $H_e < 0$. The bonding type is also determined by the.

$-\frac{G_e}{V_e}$ ratio. The bond is regarded as covalent if the ratio is less than 1 (i.e.,

$-\frac{G_e}{V_e} < 0.5$), while the interaction is thought to be totally non-covalent (weak electrostatic) for $-\frac{G_e}{V_e} > 1$[26,47]. If $0.5 < -\frac{G_e}{V_e} < 1$, the bond can be identified as partially covalent.

According to the study, the interaction of the O_3 molecule with TGC is strongly covalent resulting in a high adsorption energy. However, the dissociation of O_3 by PTGC is proved via QTAIM analysis. The O=P bond is shown to be partially covalent, whereas the O=O of O_2 gas is strongly covalent. The O_2 gas interacts with the 3rd O atom bonded with P via weak electrostatic force. The S=O bond is shown to be partially covalent, whereas the interaction of SO_2 with both TGC and PTGC is non-covalent which results in comparatively low adsorption energies.

Conclusion

Quantum dots of TGC and PTGC have been designed and optimized successfully via DFT calculations. Both structures showed real frequencies revealing the possibility of their natural existence. The sensitivity of the capsules towards O_3 and SO_2 toxic gases has been studied. O_3 reveals a comparatively stronger attraction toward both TGC and PTGC than SO_2 gas. O_3 gas dissociates to O_2 via interacting with PTGC. A significant structural deformation and charge transfer suggest a preferable adsorbate-adsorbent interaction for sensing applications. The high adsorption energies of O_3 on the adsorbents result in a huge recovery time, which makes the regenerating of TGC and PTGC via the conventional irradiation process impractical. The TGC and PTGC may recover from O_3 gas, via interacting with various regenerating agents. The charge transfer and structural deformation result in a variation of HOMO and LUMO revealing a change in the energy gap of the absorbent, which can offer an alteration of conductivity allowing the absorbents to sense the presence of toxic gases. The optical property reveals a significant shift in UV–visible spectra in the visible region due to gas adsorption, which can allow determining the nature of adsorbed gas via color change. The adsorption of O_3 and SO_2 are exothermic and endothermic process respectively where all the resulting complexes are thermodynamically stable. The QTAIM analysis reveals the nature of adsorbent-adsorbate interaction to be strong or partially covalent. The electronic and optical properties suggest both TGC and PTGC to be potential candidates for numerous optoelectronic applications. The strong adsorption energies with variation in conductivity and optical response make both TGC and PTGC potential adsorbent materials for O_3 and SO_2 gas sensing.

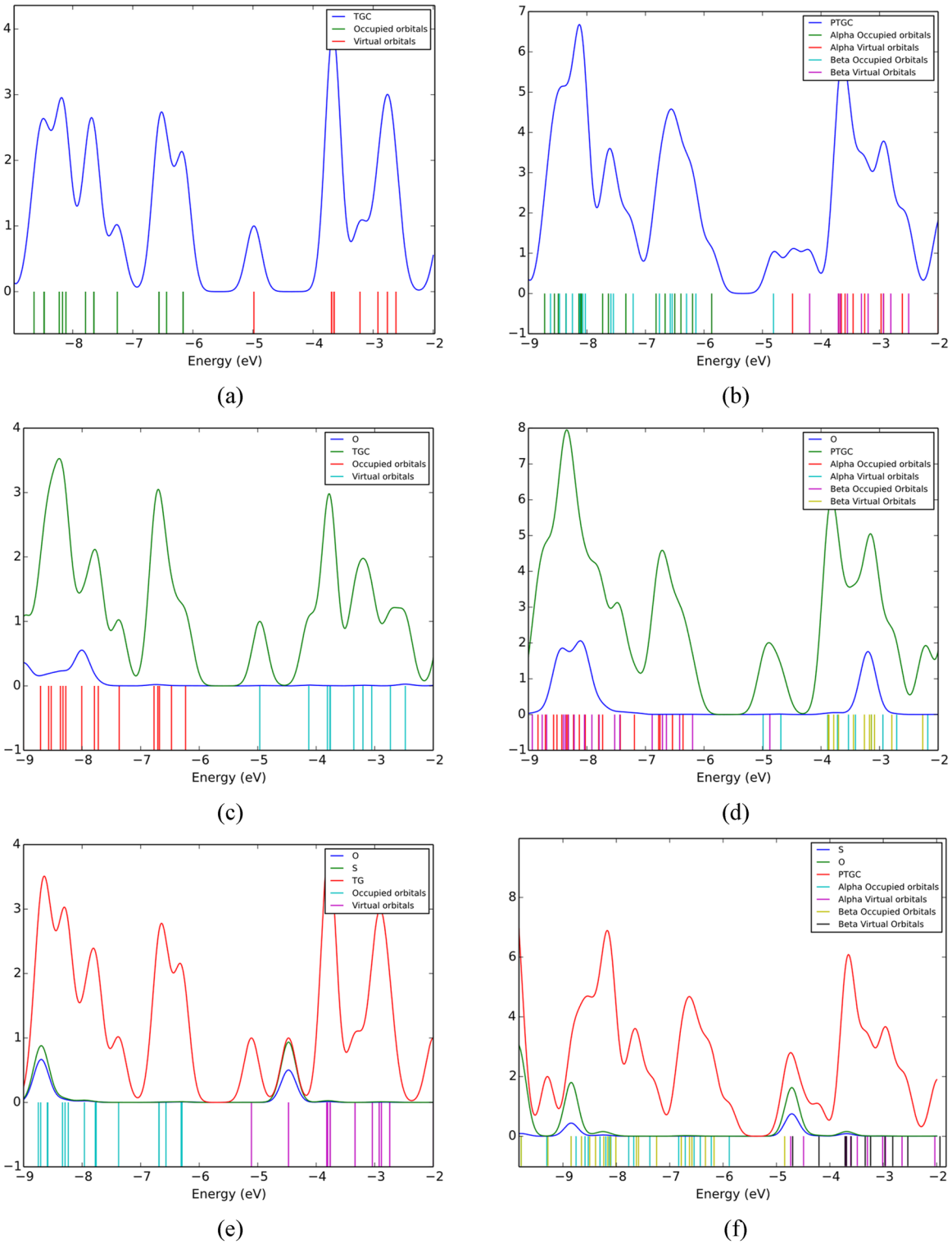

Figure 8. PDOS spectra of (**a**) TGC, (**b**) PTGC, (**c**) TGC + O_3, (**d**) PTGC + O_3, (**e**) TGC + SO_2, and (**f**) PTGC + SO_2 structures.

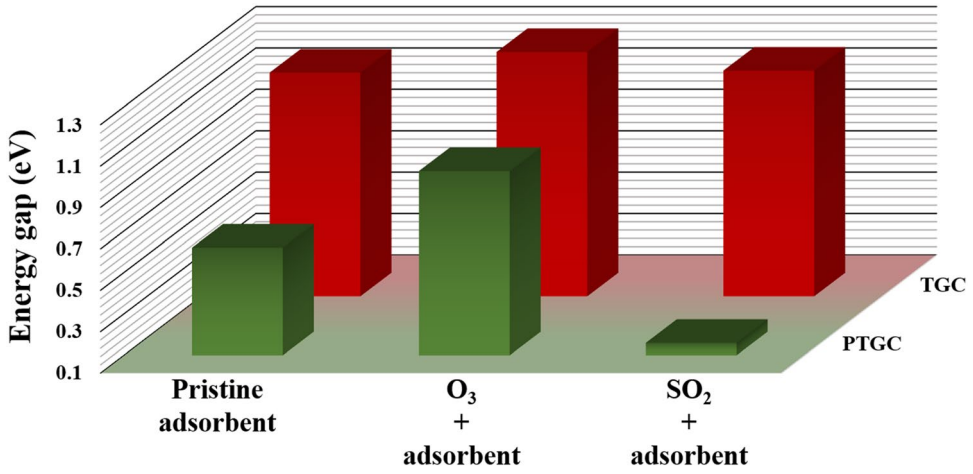

Figure 9. Variation of energy gap due to gas adsorption.

Structures	Hardness (eV)	Softness (1/eV)	Chemical potential (eV)	Electrophilicity (eV)
TGC	0.59	0.85	− 5.57	26.29
TGC + O_3	0.64	0.78	− 5.6	24.5
TGC + SO_2	0.6	0.83	− 5.71	27.17
PTGC	0.31	1.61	− 4.49	32.52
PTGC + O_3	0.5	1	− 4.38	19.18
PTGC + SO_2	0.08	6.25	− 4.77	142.21

Table 4. Global hardness, softness, chemical potential, and electrophilicity index of the structures.

Complexes	ΔH (eV/atom)	ΔG (eV/atom)	ΔS (eV/K)
TGC + O_3	− 3.15	− 2.54	− 0.0020
TGC + SO_2	0.005	0.37	− 0.0012
PTGC + O_3	− 4.07	− 3.73	− 0.0011
PTGC + SO_2	0.01	0.38	− 0.0012

Table 5. Change is enthalpy, Gibbs free energy, and entropy due to adsorption.

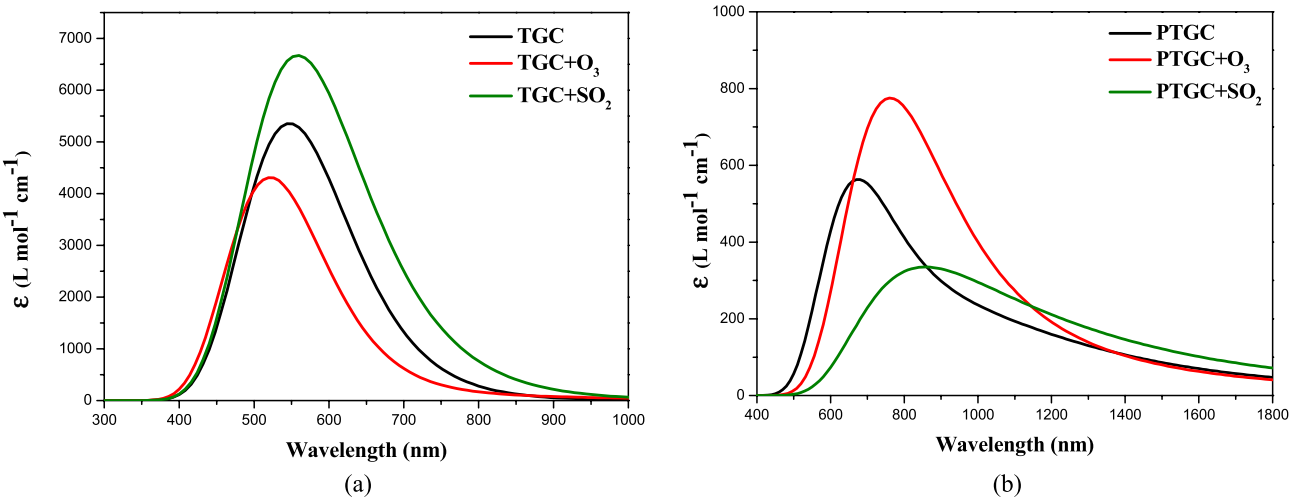

Figure 10. UV visible spectra of the adsorbents and complexes.

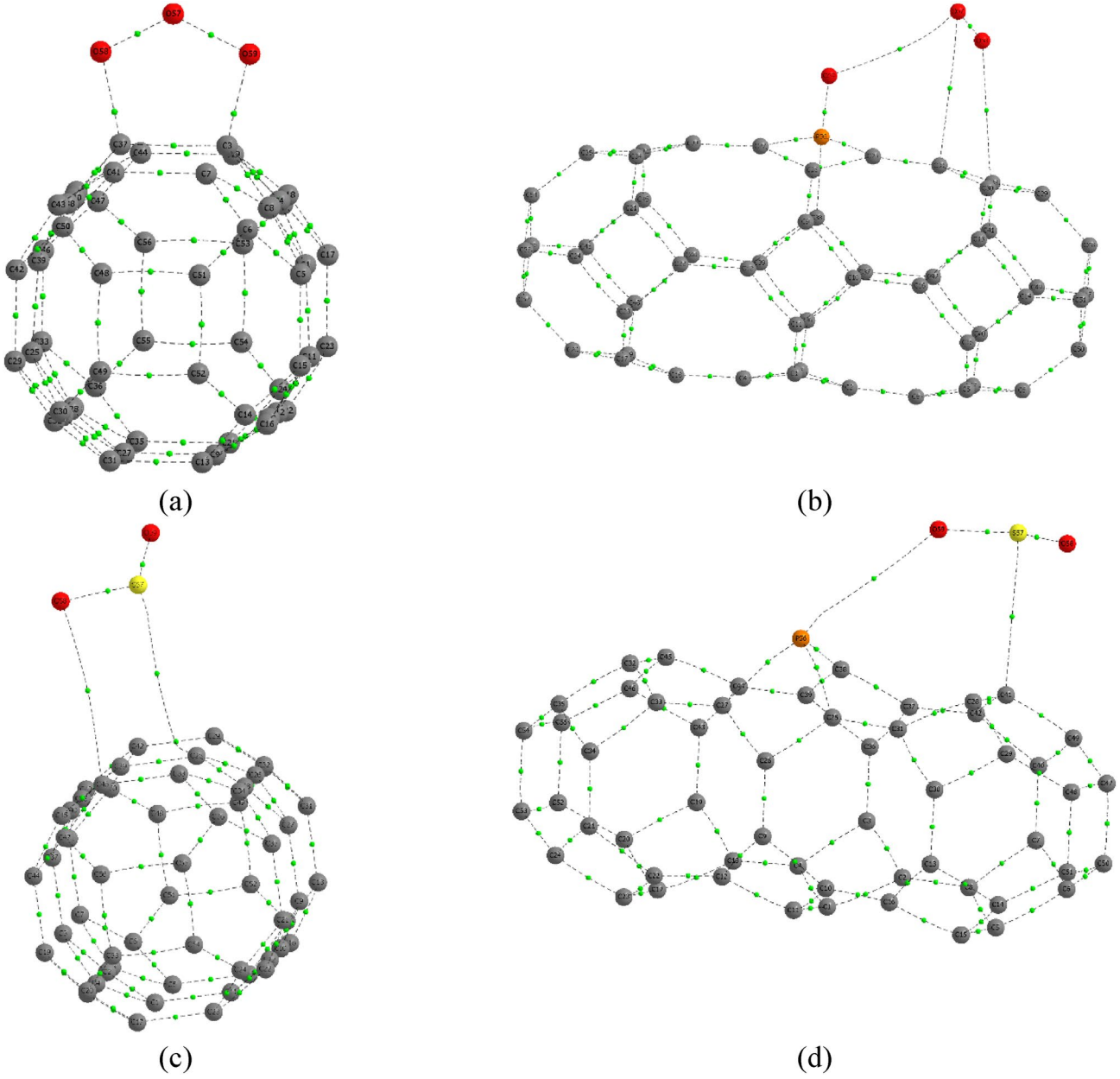

Figure 11. Molecular graph of the (**a**) TGC + O_3, (**b**) PTGC + O_3, (**c**) TGC + SO_2 and (**d**) PTGC + SO_2 complexes.

Complexes	Bonds	ρ_e	$\nabla^2(\rho_e)$	G_e	V_e	H_e	$-\frac{G_e}{V_e}$
TGC + O_3	C3–O59	0.2656	− 0.5571	0.2378	− 0.615	− 0.3771	0.3867
	C37–O58	0.2658	− 0.557	0.2384	− 0.6161	− 0.3777	0.387
	O57–O58	0.2851	− 0.0306	0.2225	− 0.4527	− 0.2302	0.4915
	O57–O59	0.2865	− 0.0345	0.2236	− 0.4559	− 0.2323	0.4905
TGC + SO_2	C46–O58	0.0023	0.0087	0.0016	− 0.0011	0.0005	1.4936
	C25–S57	0.007	0.0181	0.0035	− 0.0026	0.001	1.3861
	S57–O58	0.2738	1.2363	0.6049	− 0.9007	− 0.2958	0.6716
	S57–O59	0.2739	1.2389	0.6056	− 0.9014	− 0.2959	0.6718
PTGC + O_3	P56–O59	0.2195	1.5584	0.5306	− 0.6716	− 0.141	0.79
	O57–O58	0.5185	− 0.6462	0.4689	− 1.0993	− 0.6304	0.4265
	O59–O57	0.0059	0.0247	0.0055	− 0.0047	0.0007	1.1536
	C31–O57	0.0047	0.0179	0.0036	− 0.0028	0.0008	1.2903
	C28–O58	0.0072	0.0235	0.0051	− 0.0042	0.0008	1.192
PTGC + SO_2	P56–O59	0.0073	0.024	0.0053	− 0.0047	0.0007	1.1427
	C41–S57	0.0136	0.0386	0.0081	− 0.0065	0.0016	1.2469
	S57–O58	0.2741	1.2384	0.6059	− 0.9021	− 0.2963	0.6716
	S57–O59	0.2725	1.1996	0.5953	− 0.8907	− 0.2954	0.6683

Table 6. Electron density (ρ_e), $\nabla^2(\rho_e)$, electron's kinetic ED (G_e), potential ED (V_e), total ED (H_e), and $-\frac{G_e}{V_e}$ ratios in a.u. unit at BC point of intermolecular bonds.

Data availability

Research data is shared in the "Supplementary file".

Received: 13 December 2023; Accepted: 8 February 2024
Published online: 12 February 2024

References

1. Banibairami, T., Jamehbozorgi, S., Ghiasi, R. & Rezvani, M. Sensing behavior of hexagonal-aluminum nitride to phosgene molecule based on Van der Waals-density functional theory and molecular dynamic simulation. *Russ. J. Phys. Chem. A* **94**, 581–589 (2020).
2. Ahmed, M. T., Hasan, S., Islam, S. & Ahmed, F. First principles investigations of Cobalt and Manganese doped boron nitride nanosheet for gas sensing application. *Appl. Surf. Sci.* **623**, 157083 (2023).
3. Ahmed, M. T., Islam, S. & Ahmed, F. Density functional theory study of Mobius boron-carbon-nitride as potential CH_4, H_2S, NH_3, $COCl_2$ and CH_3OH gas sensor. *R. Soc. Open Sci.* **9**, 220778 (2022).
4. Ma, S., Yuan, D., Jiao, Z., Wang, T. & Dai, X. Monolayer Sc_2CO_2: A promising candidate as a SO_2 gas sensor or capturer. *J. Phys. Chem. C* **121**, 24077–24084 (2017).
5. Abbasi, A. & Sardroodi, J. J. Investigation of the adsorption of ozone molecules on TiO_2/WSe_2 nanocomposites by DFT computations: Applications to gas sensor devices. *Appl. Surf. Sci.* **436**, 27–41 (2018).
6. Ganji, M. D., Jameh-Bozorgi, S. & Rezvani, M. A comparative study of structural and electronic properties of formaldehyde molecule on monolayer honeycomb structures based on vdW-DF prospective. *Appl. Surf. Sci.* **384**, 175–181 (2016).
7. Ganji, M. D., Seyed-Aghaei, N., Taghavi, M. M., Rezvani, M. & Kazempour, F. Ammonia adsorption on SiC nanotubes: A density functional theory investigation. *Fuller. Nanotub. Carbon Nanostruct.* **19**, 289–299 (2011).
8. Xie, L. *et al.* A comparative study of the electronic transport and gas-sensitive properties of Graphene+, T-graphene, Net-graphene, and biphenylene-based two-dimensional devices. *ACS Sens.* **8**, 3510–3519 (2023).
9. Hou, X., Xie, Z., Li, C., Li, G. & Chen, Z. Study of electronic structure, thermal conductivity, elastic and optical properties of α, β, γ-graphyne. *Materials* **11**, 188 (2018).
10. Yu, G. *et al.* Mechanism of ozone adsorption and activation on B-, N-, P-, and Si-doped graphene: A DFT study. *Chem. Eng. J.* **430**, 133114 (2022).
11. Septiani, N. L. W. & Yuliarto, B. Review—The development of gas sensor based on carbon nanotubes. *J. Electrochem. Soc.* **163**, B97–B106 (2016).
12. Kumar, D. *et al.* Effect of single wall carbon nanotube networks on gas sensor response and detection limit. *Sens. Actuators B Chem.* **240**, 1134–1140 (2017).
13. Shetti, N. P., Mishra, A., Basu, S. & Aminabhavi, T. M. Versatile fullerenes as sensor materials. *Mater. Today Chem.* **20**, 100454 (2021).
14. Dai, J. & Yuan, J. Modulating the electronic and magnetic structures of P-doped graphene by moleculedoping. *J. Phys. Condens. Matter* **22**, 225501 (2010).
15. Shokuhi Rad, A. & Zareyee, D. Adsorption properties of SO_2 and O_3 molecules on Pt-decorated graphene: A theoretical study. *Vacuum* **130**, 113–118 (2016).
16. Ganji, M. D. & Rezvani, M. Boron nitride nanotube based nanosensor for acetone adsorption: A DFT simulation. *J. Mol. Model.* **19**, 1259–1265 (2013).
17. Bandyopadhyay, A., Paria, S. & Jana, D. Tetragonal graphene nanodot as carbon monoxide gas sensor and current rectification device. *J. Phys. Chem. Solids* **123**, 172–182 (2018).
18. Habiba, U., Piya, A. A. & DaulaShamim, S. U. Exploring the performance of T-graphene for the anode of Mg-ion and Ca-ion batteries: A first-principles study. *AIP Adv.* **13**, 115031 (2023).
19. Saedi, L., Alipour, E., Javanshir, Z. & Vahabi, V. Reversible hydrogen adsorption on Li-decorated T-graphene flake: The effect of electric field. *J. Mol. Graph. Model.* **87**, 192–196 (2019).
20. Liu, C. S., Jia, R., Ye, X. J. & Zeng, Z. Non-hexagonal symmetry-induced functional T graphene for the detection of carbon monoxide. *J. Chem. Phys.* **139**, 034704 (2013).

21. Ahmed, M. T., Roy, D., AlRoman, A., Islam, S. & Ahmed, F. A first-principles investigation of Cr adsorption on C8 and B4N4 nanocage in aqueous medium. *Phys. Chem. Chem. Phys.* **25**, 32261–32272 (2023).
22. Deng, Z. Y., Zhang, J. M. & Xu, K. W. First-principles study of SO_2 molecule adsorption on the pristine and Mn-doped boron nitride nanotubes. *Appl. Surf. Sci.* **347**, 485–490 (2015).
23. Boumya, W. *et al.* Molecular dynamic simulations and computational DFT of adsorption performances of malachite green on the metal fluorides in aqueous medium. *J. Mol. Struct.* **1270**, 133924 (2022).
24. Rahman, M. H. *et al.* $RbSnX_3$ (X = Cl, Br, I): Promising lead-free metal halide perovskites for photovoltaics and optoelectronics. *RSC Adv.* **12**, 7497–7505 (2022).
25. Sabet, M. *et al.* Theoretical assessment of the solvent effect on the functionalization of Au_{32} and C_{60} nanocages with fluorouracil drug. *Diam. Relat. Mater.* **126**, 109142 (2022).
26. Rakib Hossain, M. *et al.* First-principles study of the adsorption of chlormethine anticancer drug on C24, B12N12 and B12C6N6 nanocages. *Comput. Theor. Chem.* **1197**, 113156 (2021).
27. Mohammadzaheri, M., Jamehbozorgi, S., Ganji, M. D., Rezvani, M. & Javanshir, Z. Toward functionalization of ZnO nanotubes and monolayers with 5-aminolevulinic acid drugs as possible nanocarriers for drug delivery: A DFT based molecular dynamic simulation. *Phys. Chem. Chem. Phys.* **25**, 21492–21508 (2023).
28. Rahmanzadeh, A., Rezvani, M., Darvish Ganji, M. & Tale Moghim, M. Corrosion protection performance of Laurhydrazide N′-propan-3-one (LHP) adsorbed on zinc surface: A DFT-MD simulation investigation. *Mater. Today Commun.* **36**, 106946 (2023).
29. Mawwa, J., Shamim, S. U. D., Khanom, S., Hossain, M. K. & Ahmed, F. In-plane graphene/boron nitride heterostructures and their potential application as toxic gas sensors. *RSC Adv.* **11**, 32810–32823 (2021).
30. Roy, D., Hossain, M. R., Hossain, M. K., Hossain, M. A. & Ahmed, F. Density functional theory study of the sensing of ozone gas molecules by using fullerene-like Group-III nitride nanostructures. *Phys. B Condens. Matter* **650**, 414553 (2023).
31. Shamim, S. U. D. *et al.* Theoretical investigation of emodin conjugated doped $B_{12}N_{12}$ nanocage by means of DFT, QTAIM and PCM analysis. *Phys. E Low-Dimens. Syst. Nanostruct.* **136**, 115027 (2022).
32. Miah, M. H., Hossain, M. R., Islam, M. S., Ferdous, T. & Ahmed, F. A theoretical study of allopurinol drug sensing by carbon and boron nitride nanostructures: DFT, QTAIM, RDG, NBO and PCM insights. *RSC Adv.* **11**, 38457–38472 (2021).
33. Grabowsky, S. *Complementary Bonding Analysis* (De Gruyter, 2021). https://doi.org/10.1515/9783110660074.
34. Majidi, R. Density functional theory study on structural and mechanical properties of graphene, T-graphene, and R-graphyne. *Theor. Chem. Acc.* **136**, 1–7 (2017).
35. Rathinavel, S., Priyadharshini, K. & Panda, D. A review on carbon nanotube: An overview of synthesis, properties, functionalization, characterization, and the application. *Mater. Sci. Eng. B* **268**, 115095 (2021).
36. Rad, A. S., Shabestari, S. S., Mohseni, S. & Aghouzi, S. A. Study on the adsorption properties of O_3, SO_2, and SO_3 on B-doped graphene using DFT calculations. *J. Solid State Chem.* **237**, 204–210 (2016).
37. Rad, A. S. & Ayub, K. O_3 and SO_2 sensing concept on extended surface of $B_{12}N_{12}$ nanocages modified by Nickel decoration: A comprehensive DFT study. *Solid State Sci.* **69**, 22–30 (2017).
38. Abbasi, A. & Sardroodi, J. J. Adsorption of O_3, SO_2 and SO_3 gas molecules on MoS_2 monolayers: A computational investigation. *Appl. Surf. Sci.* **469**, 781–791 (2019).
39. Rad, A. S., Valipour, P., Gholizade, A. & Mousavinezhad, S. E. Interaction of SO_2 and SO_3 on terthiophene (as a model of polythiophene gas sensor): DFT calculations. *Chem. Phys. Lett.* **639**, 29–35 (2015).
40. Rad, A. S., Mirabi, A., Peyravi, M. & Mirzaei, M. Nickel-decorated $B_{12}P_{12}$ nanoclusters as a strong adsorbent for SO_2 adsorption: Quantum chemical calculations. *Can. J. Phys.* **95**, 958–962. https://doi.org/10.1139/cjp-2017-0119 (2017).
41. Cal, M. P., Strickler, B. W., Lizzio, A. A. & Gangwal, S. K. High temperature hydrogen sulfide adsorption on activated carbon: II. Effects of gas temperature, gas pressure and sorbent regeneration. *Carbon N. Y.* **38**, 1767–1774 (2000).
42. Hossain, M. K., Roy, D. & Ahmed, F. Boron nanocluster as a heavy metal adsorbent in aqueous environment: A DFT study. *J. Mol. Struct.* **1237**, 130302 (2021).
43. Ahmed, M. T., Islam, S. & Ahmed, F. Structural, optical, and electronic properties of boron nitride incorporated mobius carbon nanoribbon: a DFT calculation. *Phys. Scr.* **98**, 035827 (2023).
44. Muz, İ & Kurban, M. Zinc oxide nanoclusters and their potential application as CH_4 and CO_2 gas sensors: Insight from DFT and TD-DFT. *J. Comput. Chem.* **43**, 1839–1847 (2022).
45. Muz, İ, Alaei, S. & Kurban, M. Sensing capability and diameter-dependent electronic structure of boron nitride nanotubes. *Mater. Today Commun.* **27**, 102252 (2021).
46. Ahmed, M. T., Islam, S. & Ahmed, F. A-site cation replacement of hydrazinium lead iodide perovskites by borane ammonium ions: A DFT calculation. *ChemistryOpen.* **13**, e202300207 (2023).
47. Ema, S. N. *et al.* Surface adsorption of nitrosourea on pristine and doped (Al, Ga and In) boron nitride nanosheets as anticancer drug carriers: The DFT and COSMO insights. *RSC Adv.* **11**, 36866–36883 (2021).
48. Muktadir, M. G., Alam, A., Piya, A. A. & Shamim, S. U. D. Exploring the adsorption ability with sensitivity and reactivity of C_{12}–B_6N_6, C_{12}-Al_6N_6, and B_6N_6–Al_6N_6 heteronanocages towards the cisplatin drug: A DFT, AIM, and COSMO analysis. *RSC Adv.* **12**, 29569–29584 (2022).
49. Paul, D., Deb, J., Bhattacharya, B. & Sarkar, U. The influence of the substitution of transition metals on pristine C_{20}: A DFT study. *Int. J. Nanosci.* **17**, 1760026 (2018).
50. González, V. R., Escobedo-Morales, A., Cortés-Arriagada, D., de Ruiz Peralta, M. L. & Anota, E. C. Enhancement of caffeine adsorption on boron nitride fullerene by silicon doping. *Appl. Nanosci.* **9**, 317–326 (2019).
51. Xu, H. *et al.* Adsorption properties study of boron nitride fullerene for the application as smart drug delivery agent of anti-cancer drug hydroxyurea by density functional theory. *J. Mol. Liq.* **318**, 114315 (2020).
52. Kaya, S. & Kaya, C. A new method for calculation of molecular hardness: A theoretical study. *Comput. Theor. Chem.* **1060**, 66–70 (2015).
53. Kaviani, S., Tayurskii, D. A., Nedopekin, O. V. & Piyanzina, I. DFT insight into Cd^{2+}, Hg^{2+}, Pb^{2+}, Sn^{2+}, As^{3+}, Sb^{3+}, and Cr^{3+} heavy metal ions adsorption onto surface of bowl-like B30 nanosheet. *J. Mol. Liq.* **365**, 120131 (2022).
54. Shamim, S. U. D. *et al.* A DFT study on the geometrical structures, electronic, and spectroscopic properties of inverse sandwich monocyclic boron nanoclusters ConBm (n = 1.2; m = 6–8). *J. Mol. Model.* **26**, 1–17 (2020).

Author contributions

M.T.A. and A.A.R. designed materials, performed data analysis, and wrote the draft manuscript. D.R. reviewed and edited the manuscript's final version. S.I. visualized data and F.A. supervised the project.

Competing interests

The authors declare no competing interests.

Additional information

Supplementary Information The online version contains supplementary material available at https://doi.org/10.1038/s41598-024-54110-z.

Correspondence and requests for materials should be addressed to M.T.A.

Reprints and permissions information is available at www.nature.com/reprints.

Publisher's note Springer Nature remains neutral with regard to jurisdictional claims in published maps and institutional affiliations.